Functional Connectivity Shapes Spine Stability in the Hippocampus

Cynthia Rais[1] and J. Simon Wiegert[1,2,*]

[1] Research Group Synaptic Wiring and Information Processing, Center for Molecular Neurobiology Hamburg, University Medical Center Hamburg-Eppendorf, Hamburg, Germany

[2] Department of Neurophysiology, Medical Faculty Mannheim, MCTN, Heidelberg University, Ludolf-Krehl-Str. 13-17, Mannheim, Germany

* correspondence to: simon.wiegert@medma.uni-heidelberg.de

ABSTRACT

Synaptic connections between neurons determine the flow of information in the brain. Changes in synaptic weight, along with synapse formation and pruning, reshape the functional connectivity of neural circuits—key mechanisms underlying learning and memory. However, the relationship between functional strength and the structural dynamics of individual glutamatergic synapses in the living mammalian brain remains poorly understood. Specifically, how spine morphology and stability relate to functional adaptations is unclear. Here, we repeatedly recorded excitatory postsynaptic calcium transients in single postsynaptic spines of CA1 neurons in response to optogenetic stimulation of presynaptic CA3 cells in awake, head-fixed mice for over 2 weeks. We found that functional connectivity predicted both the structural stability and clustering of synaptic inputs. Spines with large responses exhibited larger volume and higher stability compared to non-responding spines. Over time, responses were highly variable at individual synapses, but stable at the dendritic level, suggesting that dendritic branches receive stable input despite large fluctuations at individual synapses.

INTRODUCTION

During learning, experience-dependent activity induces synaptic plasticity, modifying synaptic strength[1–3]. Most excitatory inputs in the brain form synapses on dendritic spines[4], where changes in synaptic strength are often accompanied by structural modifications[5–8]. This has led to the hypothesis that memory traces are stored at synapses[9,10] and, by extension, in dendritic spines. Among these, the Schaffer collateral/commissural synapses connecting the CA3 and CA1 regions of the hippocampus are considered as prototypical small glutamatergic synapses in the central nervous system. These synapses are crucial for long-term synaptic plasticity, which underlies the formation and consolidation of hippocampus-dependent declarative and episodic-like memories. The dynamic nature of memory formation and updating, particularly in response to a constantly changing environment[11] necessitates continual restructuring of neural networks[6,12]. This need for plasticity contrasts with the need for memory stability, raising a fundamental question: how does the brain maintain stable memory storage despite the inherent instability of synaptic connections. Although several candidate mechanisms have been proposed[13], the factors determining dendritic spines longevity remain only partially understood.

In the hippocampus, particularly in areas CA1, the lifetime of dendritic spines has been tracked over days to assess synaptic stability and its role in storing memory traces. However, findings remain inconsistent [14–17] with reported spine survival rates ranging from high stability to nearly complete turnover within a few weeks [17]. Many of these studies relied on repeated anesthesia, which is known to affect spine stability [15].

A major limitation of previous work is its focus on spine morphology without directly linking structural changes to synaptic function in vivo. Anatomical studies alone cannot reveal presynaptic input properties or distinguish between synaptic strength and morphological features. As a result, the relationship between connectivity strength and spine turnover in the hippocampus remains largely unexplored.

In this study, we employed chronic two-photon calcium imaging of dendritic spines in the ipsilateral CA1 (ilCA1) region of awake mice while repeatedly stimulating presynaptic contralateral CA3 (clCA3) pyramidal neurons with optogenetics. This approach allowed us to monitor localized, synaptically evoked calcium responses at individual spines and assess their functional and morphological stability over more than two weeks.

Our findings reveal that functionally active spines tend to form clusters of strongly connected spines along the same dendrite and are more stable than non-responsive spines. This suggests that robust synaptic connectivity is associated with enhanced spine persistence. Overall, our results indicate that spine lifetime in the hippocampus is closely linked to synaptic strength, which may be critical for maintaining long-term synaptic connectivity.

RESULTS

Identification of post-synaptic CA1 neurons by optogenetic stimulation of pre-synaptic CA3 neurons.

To identify ilCA1 spines connected to clCA3 neurons, we sparsely labelled ilCA1 pyramidal neurons in adult mice with a cre-dependent calcium sensor, jGCaMP7b, and implanted a chronic hippocampal window. To elicit pre-synaptic action potentials, we densely expressed the red light-activated optogenetic actuator ChrimsonR in clCA3 pyramidal neurons followed by the implantation of an optic fiber (Figure 1a, S1). During two-photon spine imaging, we recorded the motion of head-fixed mice using a passive treadmill, enabling closed-loop optogenetic stimulation selectively during periods of immobility , thereby minimizing motion artifacts (Figure 1b).

Before starting the chronic spine imaging period, we first identified ilCA1 neurons receiving synaptic input from clCA3 neurons (Figure 1c). Upon strong optogenetic stimulation in clCA3, a subset of ilCA1 neurons showed large, invariant calcium transients, while the remaining ilCA1 did not show detectable suprathreshold calcium events (Figure 1d-e). The robust and reproducible responses in individual ilCA1 cells indicate that synaptic input from optogenetically activated clCA3 neurons is reliable, without leading to unspecific, global activation of CA1. We further confirmed that optogenetically evoked synaptic input to ilCA1 was maintained constant across imaging sessions, injected five adult mice with ChrimsonR in clCA3 and non-conditional jGCaMP8m in ilCA1 for dense labelling (Figure S2a-b). In this way, we could detect the population response in ilCA1 without being biased towards a small number of sparsely labeled neurons. We stimulated clCA3 neurons using the same protocol and imaging timeline (Fig. 2c) and chronically recorded synaptically evoked calcium responses from the same population of ilCA1 neurons. We did not find any systematic changes in the mean amplitude over time, suggesting that overall optogenetically evoked synaptic transmission remained stable (Figure S2c-d). Thus, our experimental protocol enabled us to optogenetically evoke stable synaptic transmission at Shaffer commissural synapses in awake mice for weeks.

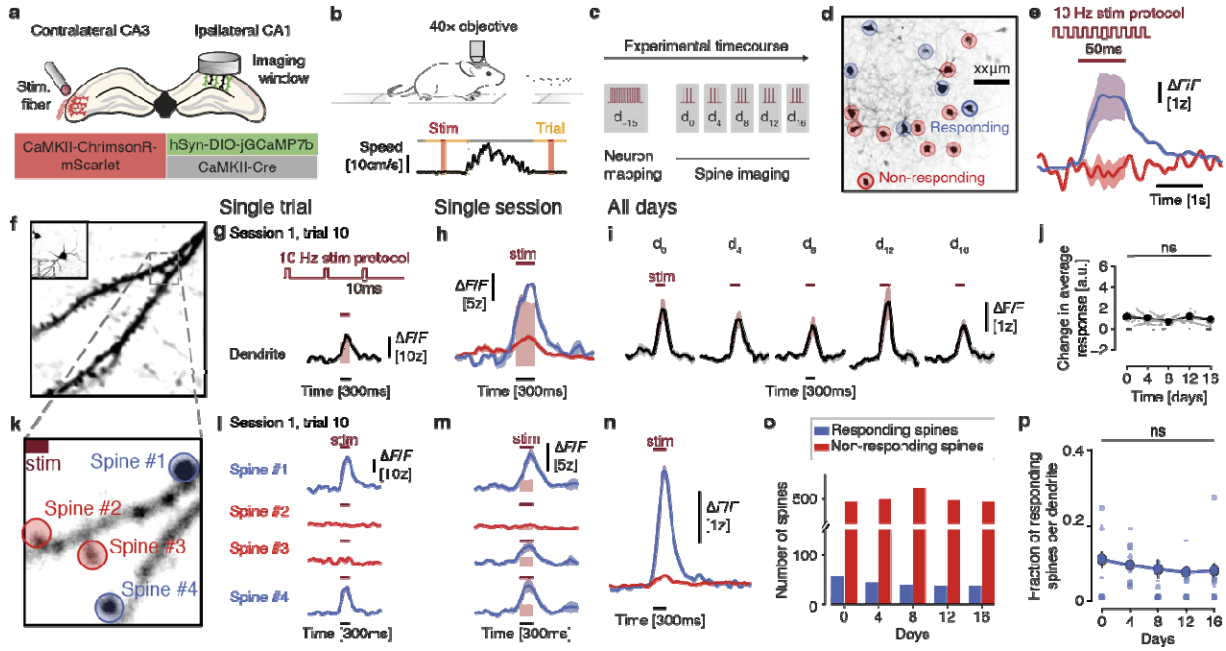

Fig. 1 Identification of synaptically connected CA1 neurons by optogenetic stimulation of pre-synaptic CA3 neurons. a) Schematic depicting injections in clCA3 and ilCA1 for sparse labelling and chronic implants for stimulation and imaging. **b)** Schematic of closed-loop, two-photon recording configuration of a mouse on a treadmill with automated motion detection. **c)** Time-course of the experiment. **d)** Example field of view with neurons responding (blue) or not responding (red) to optogenetic stimulation. **e)** Mean EPSCaTs from responding (blue) and non-responding (red) neurons in (d). Mean ± s.e.m. **f)** Example field view showing a dendrite from the neuron in the inset. **g)** Example EPSCaT in the dendrite in a single optogenetic stimulation trial. **h)** Average responses from successfully (blue) and non-successfully (red) evoked EPSCaTs in the dendrite in (f). Mean ± s.e.m. **i)** Average EPSCaTs measured at the same dendrite every four days. Mean ± s.e.m. **j)** Changes in the average amplitudes of EPSCaTs in all dendrites (gray lines). Repeated measures ANOVA. Mean ± s.e.m. **k)** Zoomed-in view of dendritic segment shown in (f) during the optogenetic stimulation trial in (g). **l)** Calcium recordings of four spines labeled in (k) during a single trial as in (g). Only spines #1 and #4 showed EPSCaTs. **m)** Average EPSCaTs from the four spines in (f) and (g). Three spines are classified as responding (blue) and one as non-responding (red) during this session. Mean ± s.e.m. **n)** Average EPSCaTs of all responding (blue) and non-responding spines (red) in one session. **o)** Number of all responding (blue) and non-responding (red) spines over time. **p)** Fraction of responding spines per dendrite over time. Repeated measures ANOVA.

Chronic imaging of postsynaptic calcium responses in single spines reveals dynamic functional connectivity

Since we aimed to investigate structural plasticity in functionally connected spines, we adjusted our optogenetic stimulation protocol such that optogenetically evoked excitatory postsynaptic calcium transients (EPSCaTs) could be identified without triggering strong global calcium transients in the entire ilCA1 neuron, which could arise from suprathreshold depolarization and action potential back propagation. The protocol was set to an intensity, such that most trials remained sub-threshold, triggering dendritic events only in a small number of trials (5.90 ± 0.90 %) (Figure 1f-h). Keeping the stimulation protocol constant, we then chronically recorded EPSCaTs in the same spines every four days over the course of 16 days (Figure 1c, S1c). To verify the reliability of our adjusted optogenetic stimulation paradigm, we first measured the average calcium transients over all trials across the entire dendrite, including suprathreshold events and all responding spines. Average calcium transients were similar across days (Figure 1i-j), validating the stability and consistency of optogenetically evoked synaptic transmission in ilCA1.

To evaluate the individual synaptically evoked calcium events for a given spine, the contribution of dendritic events was subtracted[18,19]. This method was effective in eliminating occasional weak dendritic calcium events that would lead to false-positive EPSCaTs in spines that did not receive synaptic input. We thus could identify ilCA1 spines that received inputs from

optogenetically stimulated clCA3 neurons (Figure 1k, l, S1d). As expected, spines were not showing EPSCaTs at every trial, given the low release probability of Schaffer commissural synapses. By averaging the post-synaptic responses of the entire session, we could identify ilCA1 spines receiving functional input from optogenetically stimulated clCA3 cells and discriminate them from spines never responding in that session (Figure 1m, n).

When systematically following the same spines over time (every four days), we observed that most spines responded only in one session and remained silent in preceding or following sessions. (Figure S3a, b). A small fraction of spines showed responses in two (12.0%), three (4.6%) or four (1.1%) sessions (Figure S3b). Spines showing EPSCaTs for the first time were distributed among all sessions, with a slightly higher proportion showing a first response on the first day of the experiment (Figure S3c). This variability in responses suggests that functional connectivity gets reconfigured between sessions and therefore, individual synaptic inputs drift over time.

Given the observed drift at the single-synapse level, we investigated whether the total fraction of responding spines per session remained stable across days, ensuring the preservation of average synaptic input, as suggested by the overall stability of dendritic responses (Figure 1j). Indeed, both the total number (Figure 1o) and relative dendritic fraction (Figure 1p) of responding spines remained consistent across sessions, indicating stable dendritic input. This finding is further supported by the invariant spine density across all sessions (Figure S3d).

Together, these results demonstrate that while individual synaptic inputs from clCA3 neurons exhibit high temporal variability, the overall dendritic input remains stable throughout the experiment.

Responsive spines are strongly connected to pre-synaptic partners and tend to form clusters.

Next, we asked whether ilCA1 spines that exhibited optogenetically evoked post-synaptic calcium responses at least once (termed “responsive spines”, Fig. 2a) were more strongly connected to their pre-synaptic partners than to spines that never showed any EPSCaTs (“unresponsive spines”, Fig. 2a). Spine volume is generally considered a proxy of for synaptic strength[7,20,21]. Therefore, we estimated head volumes of both responsive and unresponsive spines (Fig. 2b) and found that responsive spines were significantly larger than that of unresponsive spines (Figure 2c), suggesting that responsive spines are more strongly connected to their pre-synaptic partners. Indeed, the volume of responsive spines was positively correlated to the amplitude of EPSCaTs (Figure 2d), further supporting the idea that large spines belong to stronger synapses, as previously shown.

To ensure that our spine volume estimate was not influenced by intracellular calcium levels, we acquired volumetric stacks at an isosbestic (calcium independent) excitation wavelength (Figure S4a). We found a strong correlation between the two measures (Figure S4b-c), indicating that both strategies yielded comparable results. Additionally, we also controlled for the relationship between the volume obtained from the time-series for all spines and calcium fluctuations (Figure S4d). We did not find a significant correlation, suggesting that estimated volume was not convolved by dynamic changes in brightness due to potential calcium fluctuations.

Next, we investigated the dendritic distribution of responsive spines. Previous studies suggest that synaptic clustering can enhance local dendritic integration, potentially leading to cooperative synaptic potentiation[20,22,23]. To assess whether responsive spines exhibit clustering, we measured all-to-all dendritic distance between the spines in the field of view (Figure 2e). Our comparison of the spatial distribution of responsive and all other spines revealed a closer spatial proximity (shorter dendritic length) between responsive spines versus unresponsive spines (Figure 2f). This suggests that functional inputs from a defined population of pre-synaptic neurons are more likely to be spatially clustered rather than randomly distributed.

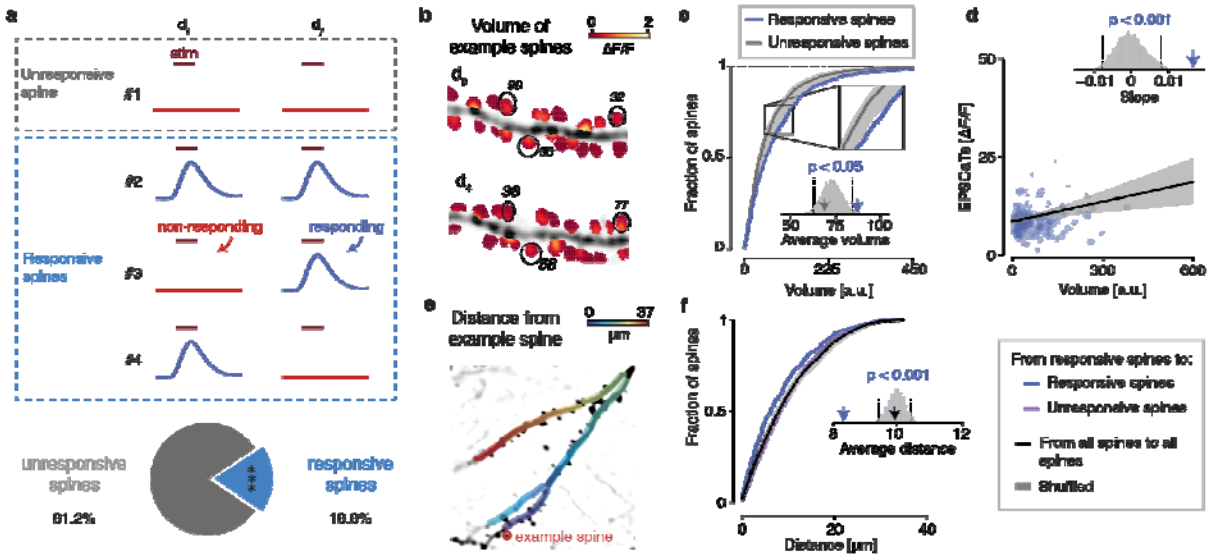

Fig 2 Responsive spines display strong synaptic connections and form clusters. a) Definition of responsive and unresponsive spines and their fractions in the total pool of analyzed spines. Top: an unresponsive spine never shows EPSCaTs (#1), while responsive spines show EPSCaTs at least once in any imaging session (#2-4). Bottom: total fraction of responsive spines. N=175 responsive spines and 754 unresponsive spines, 17 dendrites, 5 mice. Binomial test. ***: $p < 0.001$. **b)** Example of relative spine volumes on a dendrite at two different timepoints. The relative volume is derived by normalizing total spine fluorescence to dendrite fluorescence (see Methods). **c)** Cumulative distributions of spine head volumes of responsive (blue) and unresponsive (dark grey) spines. Inset: Shuffled volumes indicated by grey histogram. Arrows indicate average spine volumes. **d)** EPSCaTs amplitude as a function of the volume of responsive spines. Top: arrow indicates slope and grey histogram shows shuffled relationship between EPSCaTs and volume. **e)** Dendritic length (distance) between a given spine (example spine) and all other spines. **f)** Cumulative distributions of distances between spines. Inset: Shuffled distances indicated by grey histogram. Arrows indicate average differences between spine categories.

Responsive spines display increased stability

Since responsive spines were larger and more clustered than randomly selected unresponsive spines, we asked whether they also exhibited greater stability over time. Spines were categorized into four dynamic categories: (1) **persistent** spines, present throughout the entire time series; (2) **transient** spines, which appeared temporarily and then disappeared again; (3) **formed** spines, which emerged during the time series and remained until the end; and (4) **eliminated** spines, present at the beginning but disappearing before the end of the time series (Figure 3a).

Independently, we categorized spines as either responsive or unresponsive and analyzed their distribution across the four groups. We found that responsive spines exhibited a higher proportion of persistent spines and a lower proportion of formed spines compared to unresponsive spines (Figure 3b). Both populations contained a comparably large fraction of transient spines. However, transient spines in the responsive group were more likely to reappear at the same dendritic location on different days (i.e., they were recurrent) compared to transient unresponsive spines (Figure 3c). Recurrence was lower in the population of transient, unresponsive spines. Despite this, the frequency of flips (disappearance and reappearance) was similar between transient responsive and unresponsive spines. This recurrence in responsive spines may be explained by repeated stimulation, which could act as a stabilizing signal for the synapse, promoting the regrowth of otherwise retracting spines.

To further characterize the dynamics of responsive and unresponsive spines, we analyzed different properties related to their life expectancy in more detail. First, we assessed the turnover ratio, defined as the sum of spine formation and elimination rates between consecutive imaging sessions. Consistent with the higher fraction of persistent spines in the responsive population, the turnover ratio was consistently lower in responsive spines at each imaging interval (Figure 3d).

The turnover ratio remained invariant in both populations, indicating that optogenetic stimulation did not directly influence spine stability. This conclusion was further supported by comparing the stability of all spines in the group of optogenetically stimulated animals to spines on dendrites from control animals not undergoing optogenetic stimulation (Fig. S5). We observed no differences in the distribution of dynamic categories, the turnover ratio, or survival fraction between in the two groups (Figure S5 a-c). Thus, similar to optogenetically stimulated dendrites (Fig. S3d), the spine density on control dendrites remained stable over days (Figure S5d). Finally, spine volume was comparable between responsive, unresponsive, and control spines (Figure S5e). Together with the stable amplitude of EPSCaTs in dendrites (Figure 1i), these results confirm that the optogenetic stimulation used to identify synaptic connections did not induce significant changes in spine stability or structure over time.

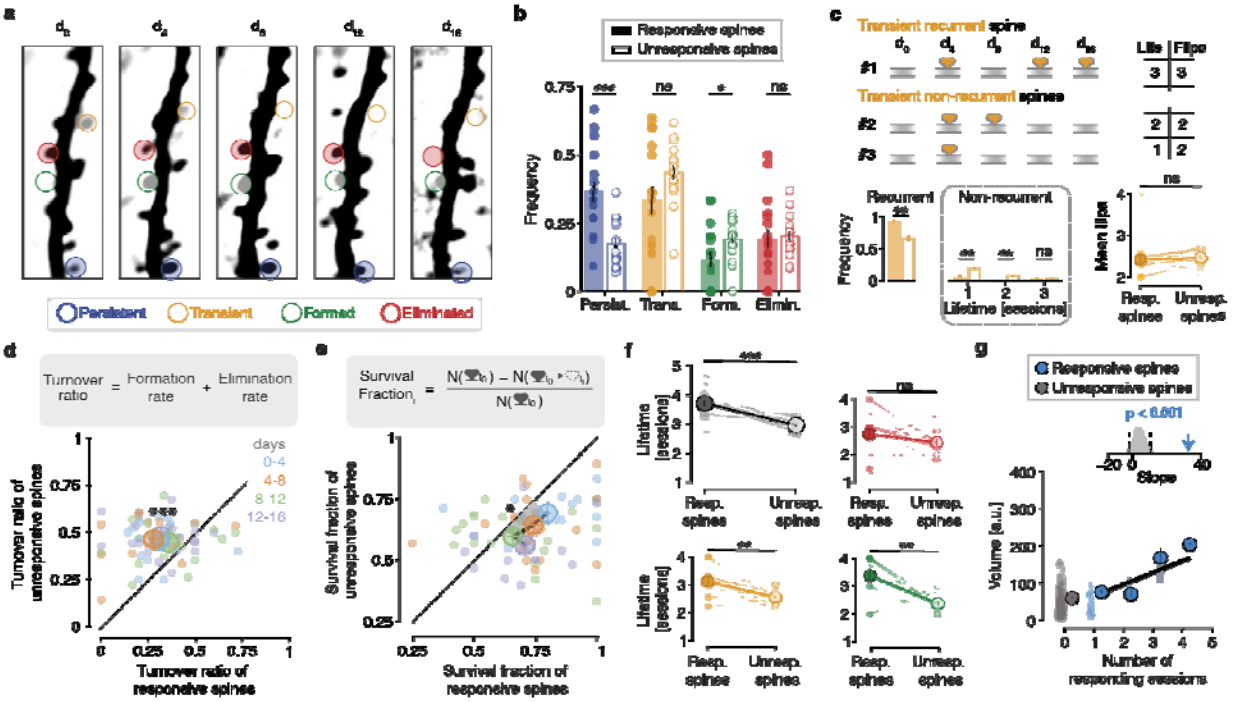

Fig. 3 Enhanced stability of responsive spines. a) Example dendrite imaged every four days. Examples of persistent (blue), formed (green), eliminated (red), transient (yellow) spines are indicated by colored circles. **b)** Frequency of the different categories for responsive (filled circles) and unresponsive spines (empty circles). Paired t-test. Each circle represents a dendrite. **c)** Characteristics of transient spines. “Life”: Cumulative lifetime in days. “Flips”: Number of appearance and disappearance events. Paired t-test with Bonferroni correction. Mean ± s.e.m. **d)** Turnover ratio of responsive spines versus unresponsive spines between two sessions. Repeated measures ANOVA. Mean ± s.e.m. **e)** Survival fraction of responsive spines versus unresponsive spines at each session. Repeated measures ANOVA. Large circles: mean ± s.e.m. Each small circle represents one dendrite. **f)** Lifetime of different types of spines for responsive (filled circles) and unresponsive spines (empty circles). Categories colored as in (b). Paired t-test with Bonferroni correction. **g)** Correlation between spine head volume and number of sessions in which the spine responded. Shuffled data indicated in shaded grey. ns: non-significant, * $p < 0.05$, ** $p < 0.01$, *** $p < 0.001$.

Consistent with the reduced number of formed spines, the formation rate of responsive spines was lower compared to unresponsive spines (Figure S6a). In contrast, the elimination rate was similar between responsive and unresponsive spines over time (Figure S6b). Both formation and elimination rates remained stable across days in both populations, in line with the observed constancy in turnover ratios. A high turnover ratio could potentially result from a high formation rate of new spines without affecting the stability of existing spines. To explore this, we assessed the survival fraction of all initially identified spines at each imaging session. The survival fraction of responsive spines was consistently higher than that of unresponsive spines, further highlighting their greater stability (Figure 3e). The increased stability and extended lifetime of responsive spines (Figure 3f) may largely be attributed to the higher proportion of persistent spines in this population. To investigate whether spine lifetime is generally higher when spines are responsive, we specifically

measured the lifetimes of all non-persistent spines. Remarkably, spines that formed during the experiment (transient and formed spines) exhibited longer average lifetimes when they were responsive to presynaptic optogenetic stimulation (Figure 3f). These findings suggest that responsive spines, which tended to be stronger than unresponsive spines, also exhibited a longer overall lifetime.

To validate this relationship independently of optogenetically identified spines, we categorized all spines—regardless of their activity—again into the four dynamics categories persistent, transient, formed, and eliminated. We then analyzed the spine volume distribution within each category, hypothesizing that persistent spines would exhibit larger volumes, indirectly suggesting that they are stronger than non-persistent ones. Across the 16-day imaging period, approximately 20% of all spines were classified as persistent (19.7%), while nearly half were transient (45.6%). The remaining spines were divided almost equally between formed (16.9%) and eliminated (17.8%) categories (Figure S7a).

As expected from the responding spine population and in agreement with previous work[21], persistent spines were significantly larger than all other non-persistent spines (Figure S7b). In contrast, transient and formed spines were smaller than the rest of the spines, in line with a lower strength and weaker integration of newly formed synapses (Figure S7c, d). In particular, the formed spines appeared to be the weakest, given their small size compared to the remaining population of spines. Eliminated spines showed no significant difference to all other spines (Figure S7e). However, since the remaining population is dominated by small formed and transient spines, this indicates that also eliminated spines tended to be smaller than persistent ones, as confirmed by their direct comparison to persistent spines (Figure S7f).

We also analyzed the spatial distribution of the four spine categories and found a shorter distance between persistent spines compared to their distance to other spines (Figure S8a), suggesting that persistent spines tended to cluster together. In comparison, no difference was found in the distance between transient spines (Figure S8b) or eliminated spines (Figure S8d). Notably, newly formed spines appeared closer to other spines than to each other (Figure S8c), suggesting that they preferably form near existing synapses.

In conclusion, persistent spines showed higher proximity to each other and were generally larger than non-persistent spines of all categories – suggesting a stronger connection to their pre-synaptic partners, while non-persistent spines were likely less strongly connected and more randomly distributed. This analysis further corroborates the positive relationship between synaptic strength, size, and stability.

Finally, we asked if the strength of the functional synaptic connection is related to spine head size. Since most spines were not showing postsynaptic responses in all imaging sessions upon optogenetic stimulation, we tested whether spine volume was correlated with the frequency of synaptic responses (i.e. the number of imaging sessions in which spines showed EPSCaTs). We found a significant positive correlation (Figure 3g) between the frequency of responses and the average volume of responding spines. Thus, our data demonstrate a close relationship between spine size, functional connectivity and spine stability at hippocampal CA3-CA1 synapses in vivo.

DISCUSSION

In this study, we demonstrate that the stability of glutamatergic spines at hippocampal CA3-CA1 synapses is dependent on connectivity strength. Using chronic two-photon imaging of spines in ilCA1 combined with optogenetic stimulation of presynaptic clCA3 neurons, we found that responsive spines exhibit increased spine size, enhanced lifetime, and greater spatial clustering compared to their neighboring spines.

Our stimulation paradigm induced local synaptic EPSCaTs in 19% of the recorded spines. The relatively low fraction of responsive spines (spines exhibiting at least one EPSCaT across imaging sessions) can be attributed to the diverse inputs received by CA1 basal dendrites, including projections from ipsilateral CA3, the amygdala, and the entorhinal cortex, which were not captured by the stimulation protocol. Notably, responsive spines exhibited EPSCaTs primarily in a single imaging session, suggesting dynamic functional reconfiguration of connectivity across sessions. This reconfiguration may reflect changes in synaptic connectivity strength, wherein fluctuations in

postsynaptic calcium responses could contribute to the transient loss of detectable EPSCaTs at weaker synapses.

Responsive spines were characterized by larger head volumes compared to non-responsive neighboring spines, indicating a stronger synaptic connection[7,20,21] with pre-synaptic clCA3 neurons. Their spatial clustering suggests that those spines could belong to functional ensembles, which previously underwent LTP[24,25] as suggested by a previous report[26]. These clustered inputs may have facilitated postsynaptic calcium responses in CA1 neurons during our initial screening (Fig. 1c-e) by lowering the response threshold[25]. The absence of calcium responses in the remaining GCaMP expressing CA1 neurons may therefore be due to a sparser distribution and low number of strongly connected synapses. This aligns with finding from a recent study demonstrating that spine clusters on place cells were correlated with the spatial tuning of these neurons during a spatial navigation task[22] Such clustering of functionally relevant spines likely contributes to neuronal firing within specific place fields, consistent with prior studies that have linked functional spine clustering to learning[20,23].

Previous research has suggested varying kinetics of spine turnover at CA1 basal dendrites[14–16]. However, these studies have only assessed anatomical features without linking spine turnover and their functional properties in vivo. By tracking functionally identified spines over more than two weeks in awake mice, we reveal that spine lifetime depends on connectivity strength. Spines with a strong functional connection (i.e. responsive spines) not only exhibited a larger head volume but also showed a lower turnover ratio, which was due to an increased survival rate and thus, an enhanced lifetime compared to their non-responding neighbors. This work is in line with a previous study, showing a correlation between spine lifetime and its size[16]. In addition to the increased stability of responsive spines we also found a correlation between the propensity of responses and spine volume, indicating that the stability of functional connectivity directly influences the weight and thereby, the persistence of a synapse, as previously suggested by anatomical studies[13,27,28].

Future studies should directly study the influence of synaptic plasticity on synapse dynamics and spine stability in the hippocampus, similar to prior in vitro research[29–31]. However, this is associated with additional challenges that occur with classical plasticity-induction protocols[31,32] such as high-frequency or burst stimulation in vivo. In our hands, such protocols strongly altered network dynamics and led to perception of this overall altered network state by the animal. This made it impossible to dissociate pathway-specific plasticity from global alterations of network states. Refined and spatially restricted stimulation protocols with better temporal control, for example, via holographic 2P-stimulation may help to overcome such limitations in the future and help to better understand the influence of long-term potentiation and depression on spine stability in vivo.

Recent studies have employed postsynaptic optogenetic stimulation of CA1 cells to induce BTSP followed by functional measurements of naturally occurring synaptic transmission[33,34]. While these studies linked synaptic plasticity to cellular function in vivo, they did not follow the functional or structural properties of these synapses over time. Thus, functional and structural studies of identified spines associated with a specific behavior or a cellular function over extended time periods will be important to shed light on the role of individual synapses in long-term information processing and storage in the brain. Indirect evidence suggests that spine stability is increased at CA1 neurons, which are part of an engram[35]. Directly assessing the lifetime of spines involved in the control of these neurons and concurrent animal behavior would provide critical insights into the synaptic mechanisms underpinning memory encoding and storage within neuronal networks.

METHODS

Animals. Adult (2 to 9 months of age) C57BL/6J mice of both sexes were used in this study. The mice originated from the Charles River company and housed in pathogen-free conditions at the University Medical Center Hamburg-Eppendorf. A light/dark cycle of 12/12 hours is used. The humidity and temperature in the room were kept constant (40% relative humidity; 20°C). Food and water were available ad libitum. All procedures were performed in compliance with German law according and the guidelines of Directive 2010/63/EU. Protocols were approved by the Behörde für Gesundheit und Verbraucherschutz of the City of Hamburg under the license numbers 32/17 and 33/19.

Mouse surgery and virus injections. C57BL/6J wild-type mice were anesthetized with 2% isoflurane/1L of O2. After 5 minutes, mice were transferred to the stereotaxic frame, and anesthesia was maintained with 1.5% isoflurane/1L of O2. To evaluate the depth of anesthesia and analgesia, the paw withdrawal reflex test was performed with a toe-pinch. Then, Buprenorphine (0.1 mg/kg) and Carprofen (4 mg/kg) were both injected subcutaneously. A heating blanket was present under the mouse throughout surgery to maintain the body temperature and eye ointment (Vidisic, Bausch + Lomb) was used to prevent eye drying. The fur on the head was trimmed and carefully removed to avoid later contamination in the surgical field. The skin was disinfected using Betaisodona. The mouse was then fixed on the stereotaxic frame and a 3-4cm midline scalp incision was made close to the injection sites. The skin was pushed to the side and a bone scarper was used for cleaning (Fine Science Tools, Heidelberg, Germany). Above the injection sites, two holes were made using a dental drill (Foredom, Bethel, Connecticut, USA). 0.3µL of AAV9-CaMKII-ChrimsonR-mScarlet-KV2.1 (AddGene # 124651-AAV9) viral suspension was first injected in left CA3 (-2.0mm AP, -2.3mm ML, -2.5mm DV relative to Bregma) using a custom-made air-pressure driven injection system. For the spine recording experiments, 0.5µL of the mix AAV9-CaMKII-Cre and AAV1-Syn-flex-jGCaMP7b-WPRE (AddGene #104493-AAV1) or AAV9-loxp- hsyn-GCaMP7b-mRuby3 was injected in right CA1 (-2.0mm AP, +1.5mm ML, -1.5mm DV relative to Bregma). In a set of experiments for cellular recording experiments, mice were instead injected with 0.5µL of AAV9-Syn-jGCaMP8m (AddGene #162375-AAV9) in CA1. The scalp was then sutured. Mice were removed from anesthesia and let recover in a clean cage on a heating blanket. For three days after surgery, mice were provided with Meloxicam mixed into soft food.

At least two weeks after virus injections, a second surgery for hippocampal window surgery took place. Mice were anesthetized as described above. After the removal of fur, the skin covering the implantation sites was removed. The skull was cleaned and roughened with a bone scraper. A first hole using the dental drill was made upon CA3 (-2.0mm AP, -3.5mm ML, titled 35° towards the left) and an optic fiber (Doric Lenses, 1.25mm ferrule diameter, 0.22 NA, 1.3 ± 0.1mm length) was inserted and glued to the skull. Once the glue dried, a circular 3mm bone piece, centered around the CA1 injection site, was carefully removed using a trephine (MW Dental, ISO 020). The dura and somatosensory cortex above the hippocampus were carefully aspirated until the apparition of the white matter tracts of the corpus callosum. Sterile PBS was used to wash the craniotomy all along, and a custom-made hippocampal imaging window was inserted. To build the window, a hollow glass cylinder was glued to a No. 1 coverslip on the bottom with UV-curable glass glue (Norland NOA61, Cranbury, New Jersey, USA). The imaging window and a head plate (Luigs & Neumann, Ratingen, Germany) were attached to the skull with cyanoacrylate gel (UHU SuperGel). Dental cement (Super Bond C&B, Sun Medical) was then applied until the complete closure of the cranial surgery. As before, animals were provided with care after the end of the surgery and could recover for at least two weeks before the beginning of experiments.

Two-photon imaging. Mice are progressively handled and habituated to the imaging setup and head fixation for at least a week before starting experiments. Additional habituation sessions were occasionally added until the mice showed no more signs of stress, usually expressed as uninterrupted and disorganized runs. Mice were placed on a linear treadmill (Luigs & Neumann, Ratingen, Germany) for close-loop experiments described below. A 633nm laser (Omicron) is connected to the implanted fiber optic on the mouse through two patch cords. From the laser combiner (Omicron, LightHUB), a main patch cord (Doric Lenses, optic fiber 200µm, NA 0.22, 2m long, SMA-SMA) is connected to a patch cord (Doric Lenses, optic fiber 200µm, NA 0.22, 1m long, SMA-MF1.25), itself connected to the implanted optic fiber through a dark mating sleeve (Doric

Lenses). To avoid light contamination from the optogenetic stimulation, a filter (Semrock, #SP01-633RU-32) is inserted before the photomultipliers, and the path between the objective and the photomultipliers is further covered with black tissue. The implanted chronic window is centered under the microscope using epifluorescence before two-photon microscopy imaging. Images were acquired with a Ti:Sa laser (Chameleon Vision-S, Coherent) tuned to 930 nm to excite jGCaMP7b and a 40× water immersion objective (Nikon CFI 40×, 0.80 NA, 3.5 mm WD, Nikon, Amsterdam, the Netherlands). Single planes (512 × 512 pixels) are acquired at 30 Hz with a resonant scanner using 10 to 40mW with ScanImage 2017b. In the first session, multiple fields of view (FOV) per mouse are acquired. For each FOV, optogenetic stimulation using a strong protocol (20 trials, 10Hz, 10 pulses of 50ms each, spaced by 5s) is used to evoke neuronal postsynaptic calcium transients. A custom Python script is used to control the laser, trigger the beginning of the session, and trigger the onset of each trial. The treadmill is continuously monitored so that if the mouse is quiet for the last second, an optogenetic trial is initiated. After post-hoc identification of responding neurons as described below, imaging of dendrites of responding neurons is performed on a subsequent session. For each session and each dendrite, subthreshold optogenetic stimulation is performed (40 trials, 10Hz, 3 pulses of 10ms each, spaced by 5s) every four days for over two weeks. The order of imaged dendrites is shuffled at the beginning of each session.

Histology. Mice were injected with a lethal dose of a mix of ketamine and xylazine and transcardially perfused with 1x PBS followed by 4% paraformaldehyde (PFA). Brains were removed and stored in 4% PFA. Brains were sliced at 60µm using a vibratome (VT1000S, Leica). Slices were mounted on microscope slides using an aqueous mounting medium (FluoroMount) and coverslips (1871, Carl Roth, Germany). Stitched images were acquired with an epifluorescence microscope (AxioObserver, Zeiss, Germany) using the 10x objective (Plan-Apochromat, Zeiss, Germany) for slice overviews and a confocal microscope (LSM 900, Zeiss, Germany) using a 20x objective (Plan-Apochromat, Zeiss, Germany) for detailed close-ups.

Data analysis

Image processing. Time series were motion-corrected using Suite2p (version 0.10.2)[36]. For dendritic imaging, t-projection from each motion-corrected recording for each day was made. T-projections were registered together using the rigid body or translation mode of the plugin StackReg[37] of the open-source platform Fiji[38]. Images were visually inspected and dendrites presenting excessive motion were removed from further analyses. Regions of interest (ROIs) were manually drawn around visually identified spines on motion-corrected frames in Fiji. ROIs were separately drawn for dendrites and the background. Calcium traces were extracted on the motion- corrected frames using a custom-made script by averaging the fluorescence of all pixels about each ROI (Macro Fiji).

Trial selection. All data were analyzed using custom-made scripts with Python (Python Software Foundation, NH, USA) installed on an open-source Anaconda environment (Anon, 2020. *Anaconda Software Distribution*, Anaconda Inc. Available at: https://docs.anaconda.com/) and the PyCharm integrated development environment (JetBrains, Prague, Czech Republic). First, residual motion present in motion-corrected recordings was identified using cross-correlation on the motion-corrected frames and excluded from the analysis. To be considered, trials required to be constituted of at least 1 second of stable baseline (without excessive motion as determined ahead), and at least 70% of the data points during stimulation need to be stable.

Fluorescent transient analysis. For cellular recording, the extracted fluorescence from Suite2p was used. To correct for fluorescence bleaching and increase the signal-to-noise ratio in the data, a baseline correction has been applied. For each neuron, the neuropil was subtracted from the raw fluorescence: $F_{neuron} = F_{raw} - 0.7 \times F_{neuropil}$ [19,36,39]. To identify neurons responding to optogenetic stimulation, for each neuron, an average trace from a baseline-corrected evoked calcium response is used. A neuron is classified as responding if more than 50% of the time points during the optogenetic stimulation are greater than 95% of the values of the mean-shuffled ΔF/F (10,000 shuffles, $p < 0.05$).

To identify dendritic transients, the distribution of the ROIs data points for each neuron was used. Using a bootstrap analysis, the null distribution was obtained by permutation of the onset of the optogenetic stimulation at random locations. Then, significant optogenetically-evoked dendritic transients were detected as ΔF/F greater than the ΔF/F obtained from the 95% of the values of the

mean-shuffled ΔF/F (10,000 shuffles, $p < 0.05$). A transient was further confirmed if, during the optogenetic stimulation, more than 30% of the data points were significant as described above.

Because suprathreshold calcium events mask the spine-specific calcium transients, robust regression is used to reduce the contamination of dendritic calcium activity on spine calcium traces, as previously reported[18,19]. To decrease the high-frequency noise in traces, spine calcium traces were convolved using a 5-bin boxcar.

For each spine, an average trace using all trials is used to determine if a spine shows excitatory postsynaptic calcium transients (EPSCaTs). As for dendrites, a spine is classified as responding if more than 30% of the time points during the optogenetic stimulation are greater than 95% of the values of the mean- shuffled ΔF/F (10,000 shuffles, $p < 0.05$). A spine is qualified as globally responding if optogenetically-evoked transients were detected in at least one out of the five sessions.

Morphological analysis. All spines were visually inspected and annotated for their existence on each day. Spines were then classified into four categories depending on the survival sequences, as follows:

- Formed if appearing on one of the sessions and staying until the end of experiments.
- Eliminated if present since the first session but disappearing from the experiments without reappearing in any of the following sessions
- Persistent if present on all recording days
- Transient if appearing and disappearing during the experimental days.

The turnover ratio was calculated as the sum of formed and eliminated spines divided by the number of spines present between the days. The survival fraction is calculated as the fraction of spines present on the given that were already existing on the first day of the experiment.

Spine densities were obtained by dividing the number of spines present on dendrites by the length of the dendritic segment.

Spine volume. The volume of each spine was estimated as previously reported[7,20]. Briefly, each t-projection was deconvolved using the plugins Diffraction PSF 3D and Iterative Deconvolve 3D[40] (Fiji). All pixels in the ROI drawn around the spine above the mean fluorescence of the background were summed and divided by the average fluorescence of the same number of pixels taken from the closest dendrite ROI.

For estimation of spine volume on the stacks obtained with the isosbestic, a z- projection is computed from the registered frames (StackReg, Fiji) excluding frames with excessive motion. The same formula is used as above for the comparison.

Spatial distribution. The interspine distances were calculated as previously reported[20]. Briefly, the distance between two spines is calculated as the dendritic length between the base of a pair of spines. The mass centers of the spines are projected on the dendrite. A path is then obtained using the Dijkstra's algorithm and the resulting distance is converted to micrometers based on a previous field of view measurement on the microscope.

Statistics. Statistical analyses were performed using custom scripts on Python or R Studio (Foundation for Statistical Computing, Vienna, Austria). Bootstrap analysis was performed with custom-made Python script when indicated, using 10,000 random permutations of the data to generate a null distribution, and significance was determined when the data points were greater than 95% of the values obtained from shuffled data ($p < 0.05$).

Repeated measures ANOVA analyses (function *aov*, stats library), Student's t- tests (function *t.test*, stats library), Pearson's chi-square tests (function *chisq.test*, stats library) and exact binomial tests (function *binom.test*, stats library) were performed using R Studio when indicated. Dendrites and mice were qualified as random effects when appropriate. Bonferroni correction was used for the paired t-test.

Data availability. The data that support the findings of this study are available from the corresponding author upon request.

Code availability. The custom code of this study is available from the corresponding author upon request.

REFERENCES

1. Whitlock, J. R., Heynen, A. J., Shuler, M. G. & Bear, M. F. Learning Induces Long-Term Potentiation in the Hippocampus. *Science* **313**, 1093–1097 (2006).

2. Xu, T. *et al.* Rapid formation and selective stabilization of synapses for enduring motor memories. *Nature* **462**, 915–919 (2009).

3. Hayashi-Takagi, A. *et al.* Labelling and optical erasure of synaptic memory traces in the motor cortex. *Nature* **525**, 333–338 (2015).

4. Harris, K. M. & Kater, S. B. Dendritic Spines: Cellular Specializations Imparting Both Stability and Flexibility to Synaptic Function. *Annu. Rev. Neurosci.* 17:341-71 (1994).

5. Nägerl, U. V., Eberhorn, N., Cambridge, S. B. & Bonhoeffer, T. Bidirectional Activity-Dependent Morphological Plasticity in Hippocampal Neurons. *Neuron* **44**, 759–767 (2004).

6. Trachtenberg, J. T. *et al.* Long-term in vivo imaging of experience-dependent synaptic plasticity in adult cortex. *Nature* **420**, 788–794 (2002).

7. El-Boustani, S. *et al.* Locally coordinated synaptic plasticity of visual cortex neurons in vivo. *Science* **360**, 1349–1354 (2018).

8. Noguchi, J. *et al.* In vivo two-photon uncaging of glutamate revealing the structure–function relationships of dendritic spines in the neocortex of adult mice. *J. Physiol.* **589**, 2447–2457 (2011).

9. Squire, L. R. *Memory and Brain*. xiii, 315 (Oxford University Press, New York, NY, US, 1987).

10. Greenough, W. T. & Bailey, C. H. The anatomy of a memory: convergence of results across a diversity of tests. *Trends Neurosci.* **11**, 142–147 (1988).

11. Fauth, M. & Tetzlaff, C. Opposing Effects of Neuronal Activity on Structural Plasticity. *Front. Neuroanat.* **10**, (2016).

12. Holtmaat, A. & Svoboda, K. Experience-dependent structural synaptic plasticity in the mammalian brain. *Nat. Rev. Neurosci.* **10**, 647–658 (2009).

13. Loewenstein, Y., Yanover, U. & Rumpel, S. Predicting the Dynamics of Network Connectivity in the Neocortex. *J. Neurosci.* **35**, 12535–12544 (2015).

14. Gu, L. *et al.* Long-Term In Vivo Imaging of Dendritic Spines in the Hippocampus Reveals Structural Plasticity. (2014) doi:10.1523/JNEUROSCI.1464-14.2014.

15. Yang, W. *et al.* Anesthetics fragment hippocampal network activity, alter spine dynamics, and affect memory consolidation. *PLOS Biol.* **19**, e3001146 (2021).

16. Pfeiffer, T. *et al.* Chronic 2P-STED imaging reveals high turnover of dendritic spines in the hippocampus in vivo. *eLife* **7**, (2018).

17. Attardo, A., Fitzgerald, J. E. & Schnitzer, M. J. Impermanence of dendritic spines in live adult CA1 hippocampus. *Nature* **523**, 592–596 (2015).

18. Iacaruso, M. F., Gasler, I. T. & Hofer, S. B. Synaptic organization of visual space in primary visual cortex. *Nature* **547**, 449–452 (2017).

19. Chen, T.-W. *et al.* Ultrasensitive fluorescent proteins for imaging neuronal activity. *Nature* **499**, 295–300 (2013).

20. Hedrick, N. G. *et al.* Learning binds new inputs into functional synaptic clusters via spinogenesis. (2022) doi:10.1038/s41593-022-01086-6.

21. Holtmaat, A. J. G. D. *et al.* Transient and persistent dendritic spines in the neocortex in vivo. *Neuron* **45**, 279–291 (2005).

22. Adoff, M. D. *et al.* The functional organization of excitatory synaptic input to place cells. *Nat. Commun.* **12**, 1–15 (2021).

549 23. Fu, M., Yu, X., Lu, J. & Zuo, Y. Repetitive motor learning induces coordinated formation of clustered
550 dendritic spines in vivo. *Nature* **483**, 92–96 (2012).

551 24. Takahashi, N. *et al.* Locally Synchronized Synaptic Inputs. *Science* **335**, 353–356 (2012).

552 25. Kastellakis, G., Cai, D. J., Mednick, S. C., Silva, A. J. & Poirazi, P. Synaptic clustering within dendrites: An
553 emerging theory of memory formation. *Prog. Neurobiol.* **126**, 19–35 (2015).

554 26. Druckmann, S. *et al.* Structured Synaptic Connectivity between Hippocampal Regions. *Neuron* **81**,
555 629–640 (2014).

556 27. Yasumatsu, N., Matsuzaki, M., Miyazaki, T., Noguchi, J. & Kasai, H. Principles of Long-Term Dynamics
557 of Dendritic Spines. *J. Neurosci.* **28**, 13592–13608 (2008).

558 28. Grutzendler, J., Kasthuri, N. & Gan, W. B. Long-term dendritic spine stability in the adult cortex.
559 *Nature* **420**, 812–816 (2002).

560 29. Roo, M. D., Klauser, P. & Muller, D. LTP Promotes a Selective Long-Term Stabilization and Clustering of
561 Dendritic Spines. *PLOS Biol.* **6**, e219 (2008).

562 30. Wiegert, J. S. & Oertner, T. G. Long-Term depression triggers the selective elimination of weakly
563 integrated synapses. *Proc. Natl. Acad. Sci. U. S. A.* **110**, (2013).

564 31. Wiegert, J. S., Pulin, M., Gee, C. E. & Oertner, T. G. The fate of hippocampal synapses depends on the
565 sequence of plasticity-inducing events. *eLife* **7**, 1–18 (2018).

566 32. Dudek, S. M. & Bear, M. F. Homosynaptic long-term depression in area CA1 of hippocampus and
567 effects of N-methyl-D-aspartate receptor blockade. *Proc. Natl. Acad. Sci. U. S. A.* **89**, 4363–4367 (1992).

568 33. Gonzalez, K. C. *et al.* Synaptic basis of feature selectivity in hippocampal neurons. *Nature* 1–9 (2024)
569 doi:10.1038/s41586-024-08325-9.

570 34. Fan, L. Z. *et al.* All-optical physiology resolves a synaptic basis for behavioral timescale plasticity. *Cell*
571 S0092867422015781 (2023) doi:10.1016/j.cell.2022.12.035.

572 35. Castello-Waldow, T. P. *et al.* Hippocampal neurons with stable excitatory connectivity become part of
573 neuronal representations. *PLoS Biol.* **18**, (2020).

574 36. Pachitariu, M. *et al.* Suite2p: beyond 10,000 neurons with standard two-photon microscopy. Preprint
575 at https://doi.org/10.1101/061507 (2016).

576 37. Thevenaz, P., Ruttimann, U. E. & Unser, M. A pyramid approach to subpixel registration based on
577 intensity. *IEEE Trans. Image Process.* **7**, 27–41 (1998).

578 38. Schindelin, J. *et al.* Fiji: an open-source platform for biological-image analysis. *Nat. Methods* **9**, 676–
579 682 (2012).

580 39. Peron, S. P., Freeman, J., Iyer, V., Guo, C. & Svoboda, K. A Cellular Resolution Map of Barrel Cortex
581 Activity during Tactile Behavior. *Neuron* **86**, 783–799 (2015).

582 40. Dougherty, R. Extensions of DAMAS and Benefits and Limitations of Deconvolution in Beamforming |
583 Aeroacoustics Conferences. *Adv. Test. Tech. Phased Arrays* (2012) doi:https://doi.org/10.2514/6.2005-2961.

584

585

ACKNOWLEDGMENTS

We thank Stefan Schillemeit and Kathrin Sauter for excellent technical support, Maxime Maheu for help with data analyses, Wei Yang for initial training on spine imaging. Ingke Braren of the UKE Vector Facility produced rAAV vectors. This work was supported by European Research Council (ERC2016-StG-714762 to J.S.W.) and the German Research Foundation, DFG (FOR2419/P6, to J.S.W.).

AUTHOR CONTRIBUTIONS

C.R. and J.S.W. designed the experiments and wrote the manuscript. C.R. performed the experiments and analyzed the data. J.S.W. acquired funding and supervised the study.

SUPPLEMENTAL FIGURES

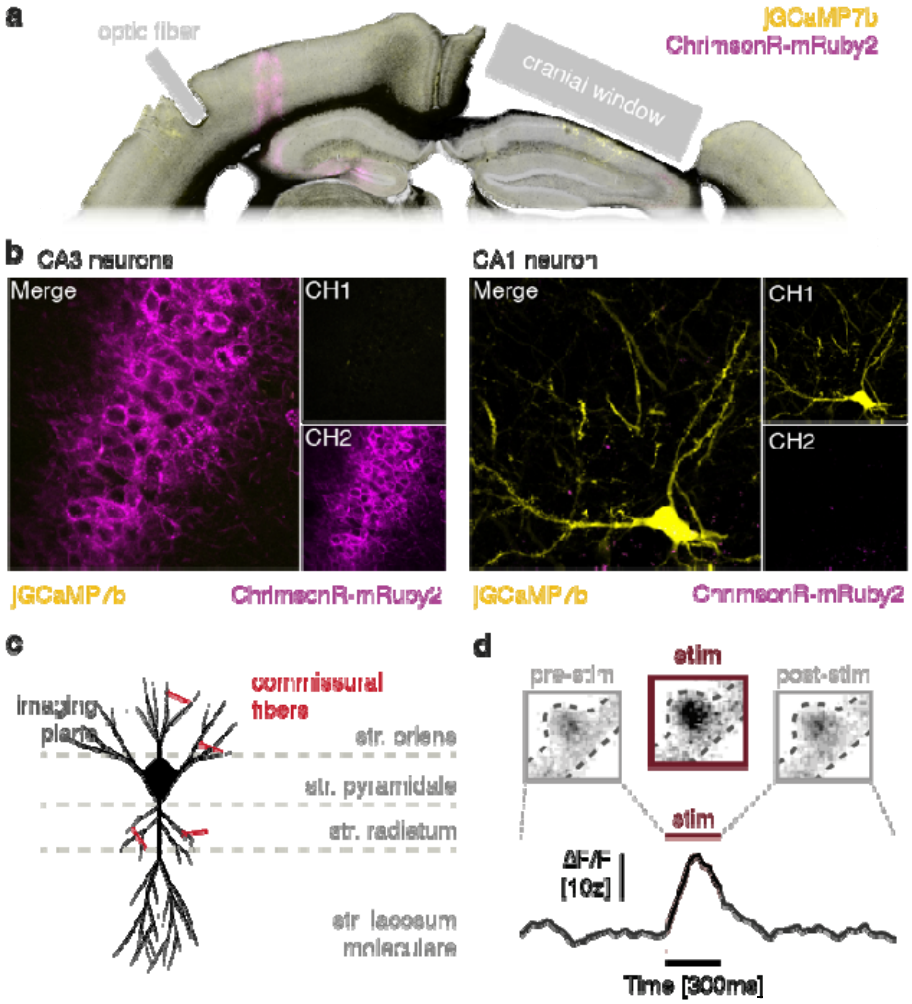

Fig. S1. Imaging of spines in CA1. a) Histology. clCA3 neurons express ChrimsonR-mRuby2 (magenta). ilCA1 are sparsely expressing jGCaMP7b (yellow). An optic fiber for stimulation is placed above clCA3 and a chronic imaging window is implanted above ilCA1. **b)** Confocal images of clCA3 and ilCA1 expressing neurons. ChrimsonR-mRuby2 and jGCaMP7b are shown in magenta (CH2) and yellow (CH1), respectively. **c)** Schematic drawing of an ilCA1 neuron showing the imaging plane in stratum oriens. **d** Example calcium trace of a single EPSCaT with corresponding t-projections of the spine before, during and after optogenetic stimulation.

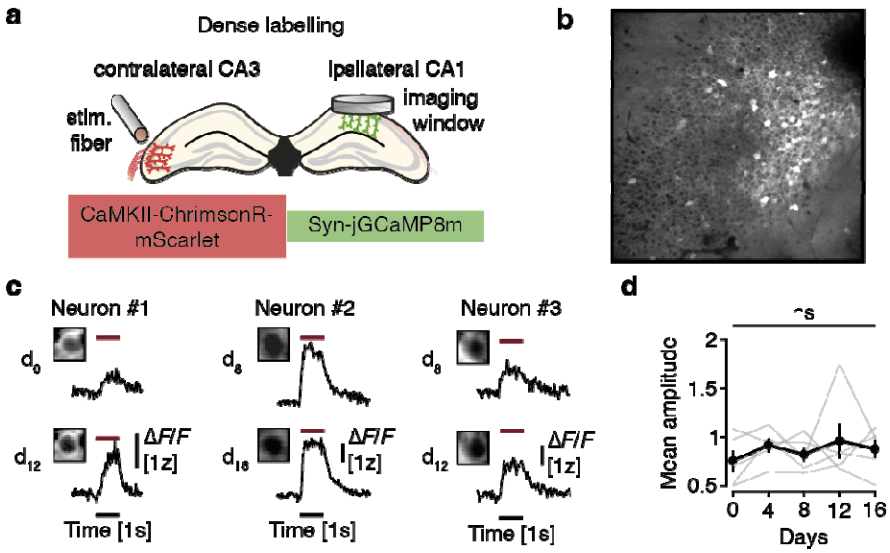

Fig S2. Stable optogenetic stimulation of ilCA1 over the time course of the experiment. a) Schematic depicting the injections and chronic implants for dense labelling of ilCA1 with jGCaMP8m. **b)** Example field of view with densely labelled neurons in ilCA1. **c)** Average postsynaptic calcium responses from three example neurons at two timepoints (d0 and d12). **d)** Average mean amplitude of postsynaptic calcium responses over the time course of the experiment for all responding neurons (n = 5 mice, 387 neurons). Repeated measure ANOVA. ns: non-significant. Mean ± s.e.m.

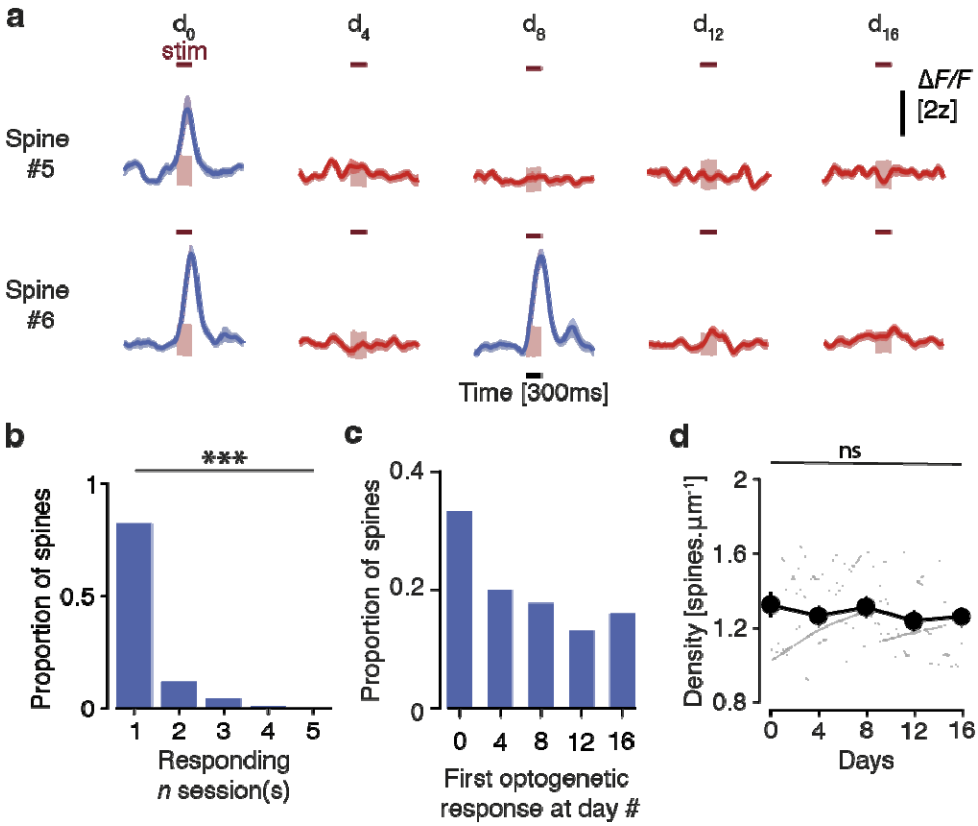

Fig. S3. The majority of responsive spines show EPSCaTs only in one session. a) Examples of responding status changes over time. Spine #5 was responding in one session (d0) while spine #6 was responding in two sessions at days 0 and 8. Mean ± s.e.m. **b)** Distribution of spines according to the number of sessions in which they showed a response. Chi- square test. **c)** Distribution of spines according to the sessions in which they showed a response for the first time. **d)** Average spine density on all recorded dendrites. Repeated measures ANOVA.Ns: non-significant Mean ± s.e.m.

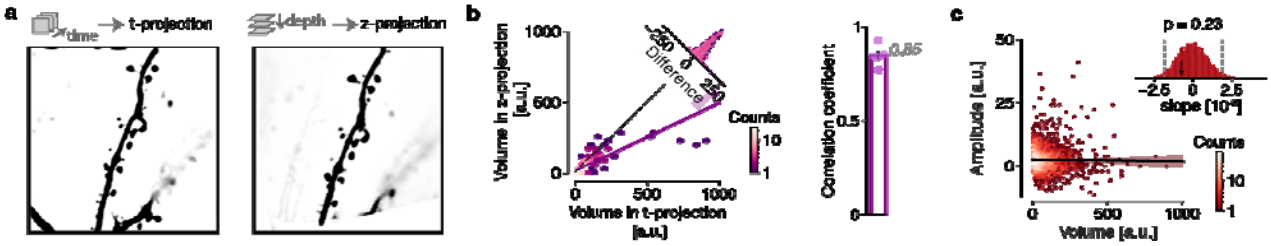

Fig. S4. Spine volume estimated from the time series is independent of calcium activity. a) Example projections of the same dendrite from the time-series (t-projection) and from the stack (z-projection). **b)** Correlation between the volume evaluated from z-projections and the volume from t-projections for all spines (n=164 spines, 4 dendrites, 5 sessions). **c)** Correlation between head volume of spines and the amplitude of EPSCaTs. Null distribution of slopes. ***: $p < 0.001$.

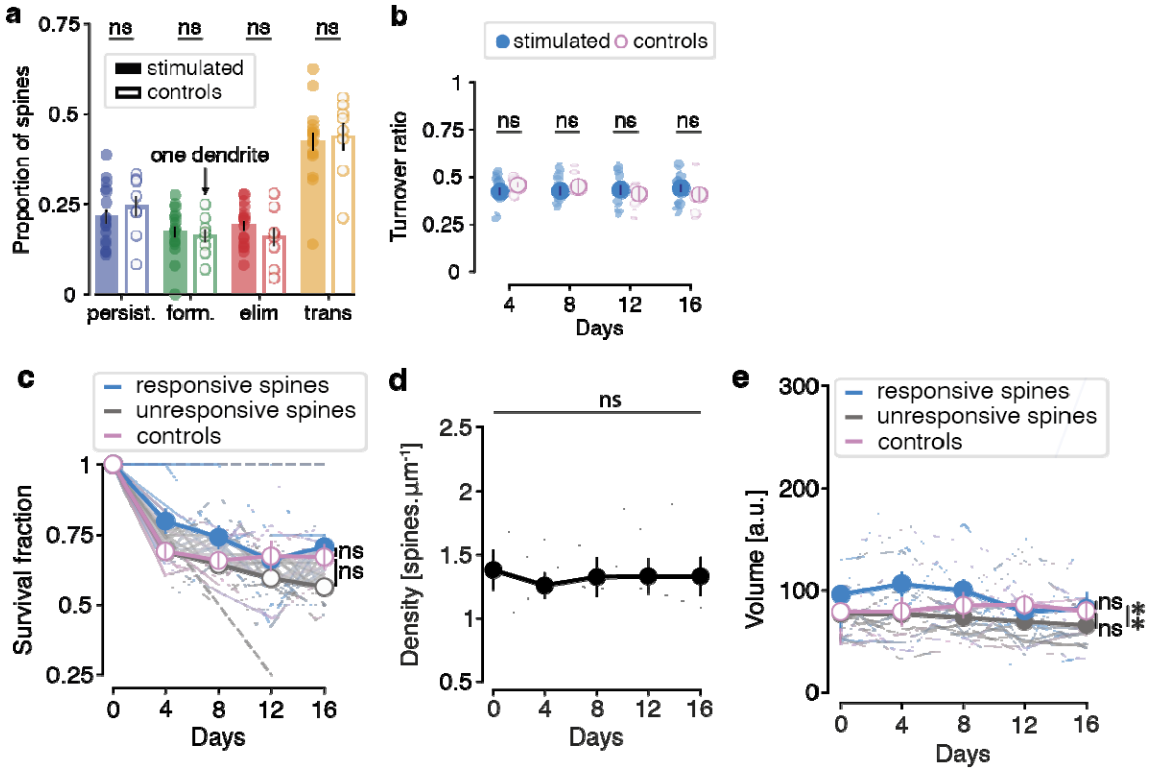

Fig. S5. Optogenetic stimulation does not affect the overall stability or volume of dendritic spines. a) Proportion of different dynamic spine categories on dendrites in control animals (no optogenetic stimulation) and optogenetically-stimulated animals. Unpaired t-test. N = 8 dendrites. Mean ± s.e.m. Each dot represents a dendrite. **b)** Turnover ratio of stimulated dendrites and controls over time. Welch unpaired t-test **c)** Survival fractions of control, responsive and unresponsive spines. Repeated measures ANOVA. **d)** Density of spines for control animals. Repeated measure ANOVA. **e)** Volume of spines for control, responsive and unresponsive spines. Repeated measure ANOVA. ns: non-significant.

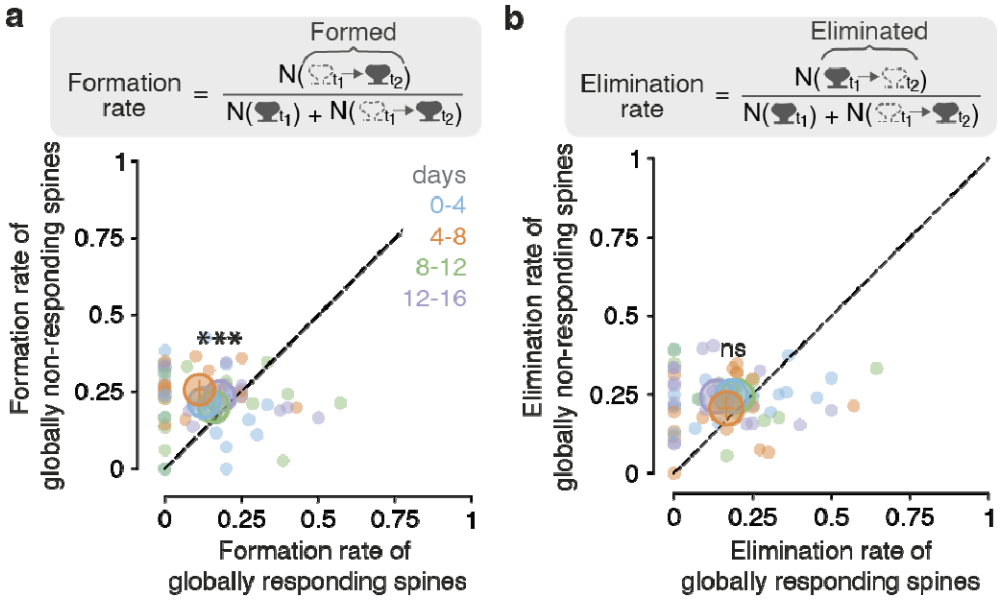

Fig S6. Spine turnover of responding spines is exclusively influenced by the formation rate. a) Formation rate and **b)** elimination rate of responsive spines versus unresponsive spines over time. Repeated measures ANOVA. Mean ± s.e.m.

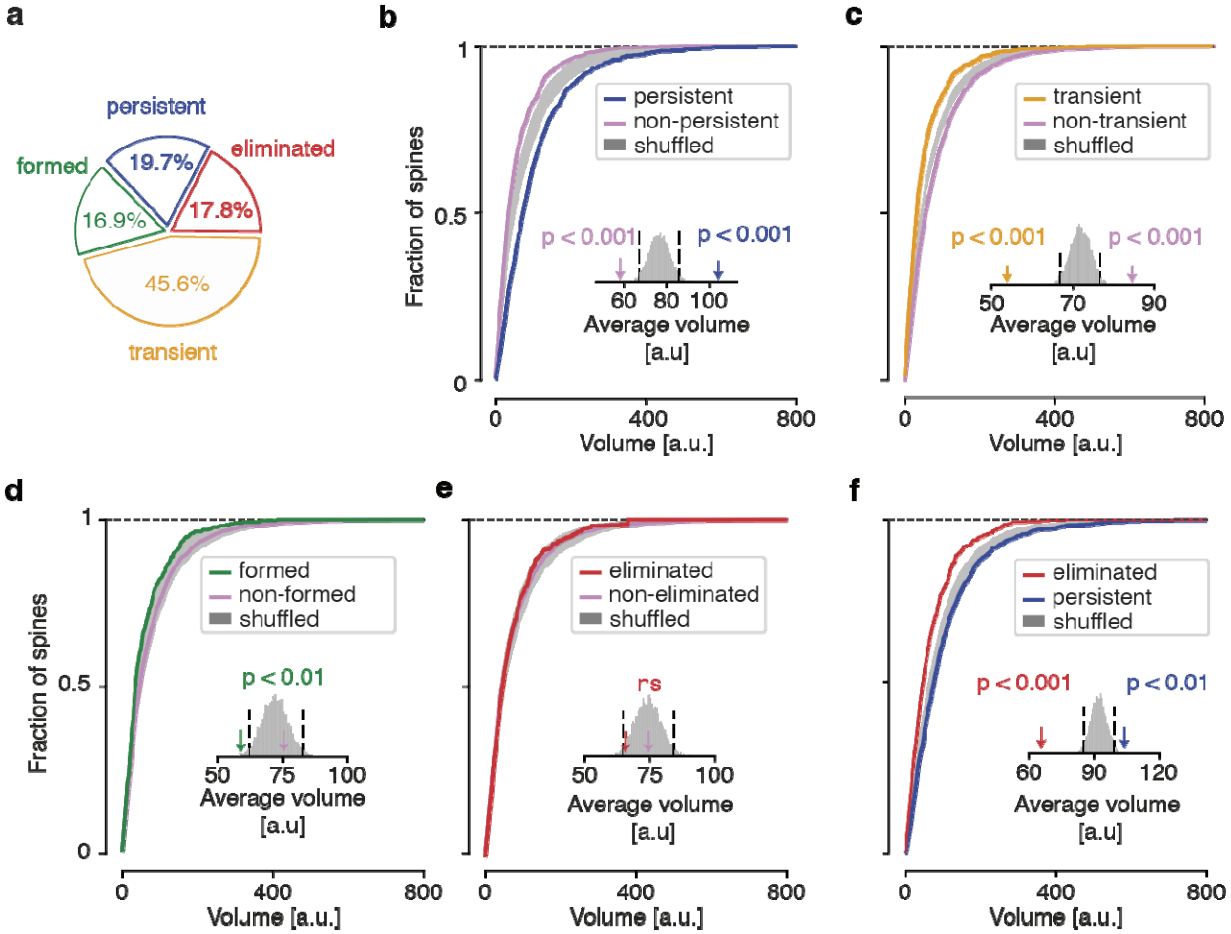

Fig S7. Stable spines have larger head volumes. a) Percentages of the different dynamic spine categories. **b) - e)** Cumulative distributions of the head volumes of persistent (**b**), transient (**c**), formed (**d**) and eliminated (**e**) versus spines of all other categories (pink). **f)** Cumulative distributions of the head volumes of persistent versus eliminated spines. Shuffled volumes are indicated in shaded grey. Arrows indicate actual average spine volumes of the respective categories.

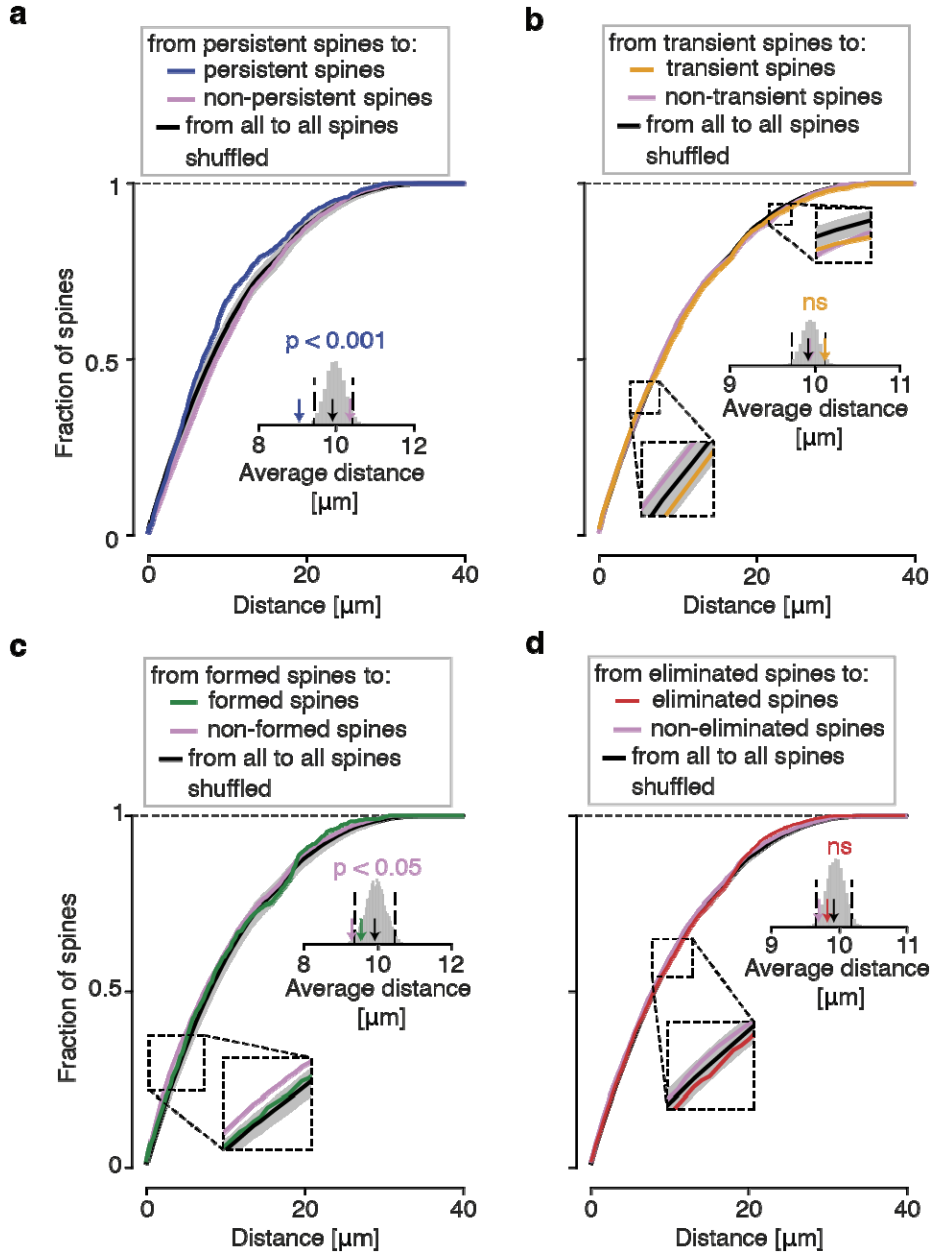

Fig S8. Persistent spines show higher proximity to each other than non-persistent spines. a) - d) Cumulative distributions of distances between persistent spines, transient spines, formed spines and eliminated spines compared to the distances to the other spines. Shuffled distances are indicated in shaded grey. Shuffled distances are indicated in shaded grey. Arrows indicate actual average distance between spines of the respective categories.